





Cite this: *Soft Matter*, 2025, 21, 7786

# Chirality and concentration govern polycatecholamine self-assembly: a comparative study of dopamine, levodopa, and norepinephrine

Alexander J. Steeves <sup>ab</sup> and Fabio Variola <sup>\*abcd</sup>

Polycatecholamines (pCAs), including poly(dopamine) (pDA), poly(levodopa) (pLD) and poly(norepinephrine) (pNE), hold enormous potential in biomaterials science in the form of functional coatings and particles due to their adhesive and versatile physicochemical properties. However, while pDA has been extensively studied, the potential of pLD and pNE has yet to be fully explored. To bridge this gap, this study provides a comparative analysis of dopamine (DA), levodopa (LD), L-norepinephrine (L-NE), and racemic norepinephrine (rac-NE), focusing on how precursor chemistry, concentration (0.5 vs. 2.0 mg mL<sup>-1</sup>), and NE chirality influence polymerization kinetics and particle formation. By employing dual-wavelength absorbance (450 nm,  $A_{450}$ ; 600 nm,  $A_{600}$ ) measurements, we revealed distinct concentration-dependent effects, with higher concentrations accelerating monomer-to-intermediate transitions and inducing saturation kinetics. Dynamic light scattering (DLS) highlighted particle size evolution, showing how the zwitterionic character of pLD and chirality in pNE affect stability and size distribution. Additionally, we introduced the polymer dispersion ratio (PDR), a novel metric mapping spatial and temporal aggregate distribution, identifying distinct aggregation and sedimentation patterns. Results from this study underscore the critical role of precursor concentration and chirality in shaping the properties of pCA coatings, namely the temporal evolution of the surface-deposited polymer. Ultimately, this framework informs the synthesis and selection of pCAs for biomedical applications, including functional (e.g., cell-instructive, antibacterial) coatings with tailored topography for implantable devices, drug-eluting platforms, and bioadhesive technologies, while also translating to broader research areas which could benefit from these findings, such as energy storage and environmental remediation, among others.

Received 10th July 2025,  
Accepted 31st August 2025

DOI: 10.1039/d5sm00718f

[rsc.li/soft-matter-journal](http://rsc.li/soft-matter-journal)

## Introduction

Catecholamines (CAs) are bioactive molecules characterized by a catechol group and an ethylamine side chain, primarily functioning as neurotransmitters within biological systems. Among these, dopamine (DA) has attracted significant attention in biomaterials research due to its ability to polymerize into poly(dopamine) (pDA), a functional material with robust adhesive properties and exceptional versatility for various biomedical applications.<sup>1–4</sup> The oxidative polymerization of DA results in a eumelanin-like material composed of conjugated oligomers and polymers. This material can be deposited on a wide range of substrates, including metals, polymers and ceramics.<sup>2</sup> This

versatility is enhanced by pDA's diverse molecular interactions, including cation- $\pi$ , anion- $\pi$ ,  $\pi$ - $\pi$ , covalent, van der Waals, and hydrogen bonding, which render it a flexible alternative for bioactive coatings, drug delivery systems and antibacterial surfaces.<sup>5–8</sup>

While pDA remains a cornerstone of applied biomaterials, other catecholamines such as levodopa (LD) and norepinephrine (NE) are emerging as promising alternatives.<sup>9</sup> In particular, poly(levodopa) (pLD) and poly(norepinephrine) (pNE) exhibit unique physicochemical properties and distinct polymerization characteristics, which broaden their employment in specialized biomedical and technological contexts. For instance, pLD has been utilized in antibacterial wound dressings, molecularly imprinted sensors for pesticides, and enantioselective coatings for chromatographic applications.<sup>10–12</sup> Similarly, pNE has demonstrated significant potential in enhancing neural adhesion and neurite extension, making it suitable for neuroengineering applications.<sup>13–16</sup>

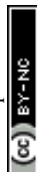
Notably, the focus of many biomedical applications lies in creating uniform functional coatings and films, capitalizing on

<sup>a</sup> Faculty of Engineering, Department of Mechanical Engineering, University of Ottawa, Ottawa, ON, Canada. E-mail: [fabio.variola@uottawa.ca](mailto:fabio.variola@uottawa.ca)

<sup>b</sup> Ottawa-Carleton Institute for Biomedical Engineering (OCIBME), Ottawa, Canada

<sup>c</sup> Faculty of Medicine, Department of Cellular and Molecular Medicine, University of Ottawa, Ottawa, ON, Canada

<sup>d</sup> Children's Hospital of Eastern Ontario (CHEO), Ottawa, ON, Canada



the fact that the oxidative polymerization process inherently leads to the formation of polycatecholamine (pCA) aggregates in suspension, ranging from nanoparticles (NPs) to microparticles ( $\mu$ Ps). The subsequent precipitation of these aggregates on the substrate creates micro- and nano-topographical features that may be harnessed to control cell–substrate interactions and antibacterial properties.<sup>17–19</sup> In fact, the topography at the micro- and nano-scale influences how cells adhere, proliferate, and differentiate, while also determining the substrate's ability to resist bacterial colonization.<sup>18,20,21</sup> In addition to the rational design of the topography of surface coatings, controlling the characteristics of the suspended particles, particularly their size, is equally critical as it directly influences key functions for additional biomedical contexts making it a pivotal factor in engineering advanced therapeutic platforms.

The ability to create cell-instructive topographies using pDA aggregates is well-established,<sup>18,20,21</sup> yet this level of control has not been extended to coatings derived from additional pCAs. The full potential of these alternative precursors can only be unlocked through a deeper understanding of their polymerization. For example, recent work has shown that precisely guiding polymerization to form highly ordered nanofibers can yield materials for advanced applications like electromagnetic shielding.<sup>22</sup> Achieving such control for pNE and pLD requires fundamental knowledge of how precursor chemistry, concentration, and chirality govern particle formation and aggregation. This foundational understanding enables researchers to move beyond trial-and-error by providing the metrics and comparative data needed to achieve the predictive control necessary to rationally design and engineer these functional materials.

The structural differences among DA, LD and NE significantly influence their polymerization and properties. LD and NE introduce additional functional groups on the  $\beta$ -carbon of the ethylamine side chain: carboxyl ( $-\text{COOH}$ ) for the former and hydroxyl ( $-\text{OH}$ ) for the latter. These functional groups alter intermolecular interactions and impart chirality, enabling enantioselective polymerization under enzymatic conditions, as demonstrated in studies on L-, D-, and racemic-DOPA.<sup>23</sup> In this context, such chiral specificity profoundly enhances polymerization efficiency and material properties, as racemic systems demonstrate superior molecular packing, thermal stability, and mechanical strength.<sup>23</sup> However, in the context of pNE, literature reveals a lack of consensus on its enantiomeric composition; studies have variably utilized the L-enantiomer (L-NE),<sup>14,16,24–26</sup> a racemic mixture (rac-NE),<sup>13,27–29</sup> or have not indicated the chirality.<sup>9,15,30–33</sup> Polymerization of these precursors yields distinct materials, namely poly(L-norepinephrine) (pLNE) and poly(rac-norepinephrine) (pRNE). This ambiguity, coupled with limited data on how NE chirality may impact the auto-oxidative polymerization kinetics and the resulting material properties (e.g., particle size, aggregation behaviour, surface chemistry), underscores the need for a systematic investigation. Additionally, while precursor concentration is a central variable influencing pDA synthesis, kinetics, particle size and aggregation dynamics, the influence of this variable remains underexplored for pLD and pNE.<sup>34,35</sup>

To address this gap, our study provides a comparative analysis of DA, LD, L-NE and rac-NE polymerization under controlled conditions, focusing on the effects of precursor chemistry, concentration and the chirality of NE on polymerization kinetics and particle formation. Specifically, our analysis focused on two distinct concentrations: a low precursor concentration of  $0.5 \text{ mg mL}^{-1}$  and a high concentration of  $2.0 \text{ mg mL}^{-1}$ . These concentrations were selected to encompass the critical threshold ( $1.0\text{--}2.0 \text{ mg mL}^{-1}$ ), where significant transitions in film thickness, particle size, and aggregation dynamics have been previously observed for pDA.<sup>35,36</sup> By explicitly comparing L-NE and rac-NE, we aim to elucidate how stereochemistry influences the auto-oxidative polymerization and resulting characteristics of pNE particles and aggregates.

Polymerization kinetics were evaluated through absorbance-based measurements at  $450 \text{ nm}$  ( $A_{450}$ ) and  $600 \text{ nm}$  ( $A_{600}$ ), a well-established approach to provide insight into the complex polymerization and structural dynamics of pCA materials during polymerization.<sup>23,37,38</sup> Dynamic light scattering (DLS) analysis offered a quantitative examination of the  $\mu\text{P}$  ( $> 100 \text{ nm}$ ) and NP ( $\leq 100 \text{ nm}$ ) diameters, detailing the temporal progression of particle size from the initial stages through  $24 \text{ h}$  post-initiation. Furthermore, to capture the macroscopic aggregation and sedimentation behaviour often overlooked by standard kinetic or particle sizing techniques, we introduced the polymer dispersion ratio (PDR), a novel metric designed to quantify spatial distribution and aggregation uniformity within the deposited materials. Ultimately, by integrating absorbance kinetics with particle size analysis, we established a comprehensive framework to examine the effects of precursor concentration and chirality on polymerization behaviour. Understanding these aggregation dynamics is particularly important given that cells interact directly with pCA aggregates,<sup>21</sup> influencing the design and efficacy of potential cell-instructive coatings based on these materials.

Our findings reveal the link among molecular structure, polymerization kinetics and particle formation/deposition, contributing to strengthen the required fundamental knowledge for the rational design of pCA-based functional surfaces and micro/nano-sized particles for biomedical applications by elucidating the roles of concentration and chirality.

## Results and discussion

### Absorbance kinetics and polymerization dynamics of polycatecholamines (pCAs)

To elucidate the polymerization kinetics of the polycatecholamines considered in this study, dual-wavelength absorbance measurements at  $450 \text{ nm}$  ( $A_{450}$ ) and  $600 \text{ nm}$  ( $A_{600}$ ) were utilized (Fig. 1). In particular, the evolution of these materials underpins the selection of  $A_{450}$ , which has been similarly used to measure the formation of DA, NE, and LD-derived materials and compare early-to-late-stage products of DA.<sup>38,39</sup> Specifically, signals in the  $400\text{--}500 \text{ nm}$  range are associated with the formation of less complex oligomers (e.g., DA–DA) as indicated by both theoretical (e.g., density functional theory [DFT]) and



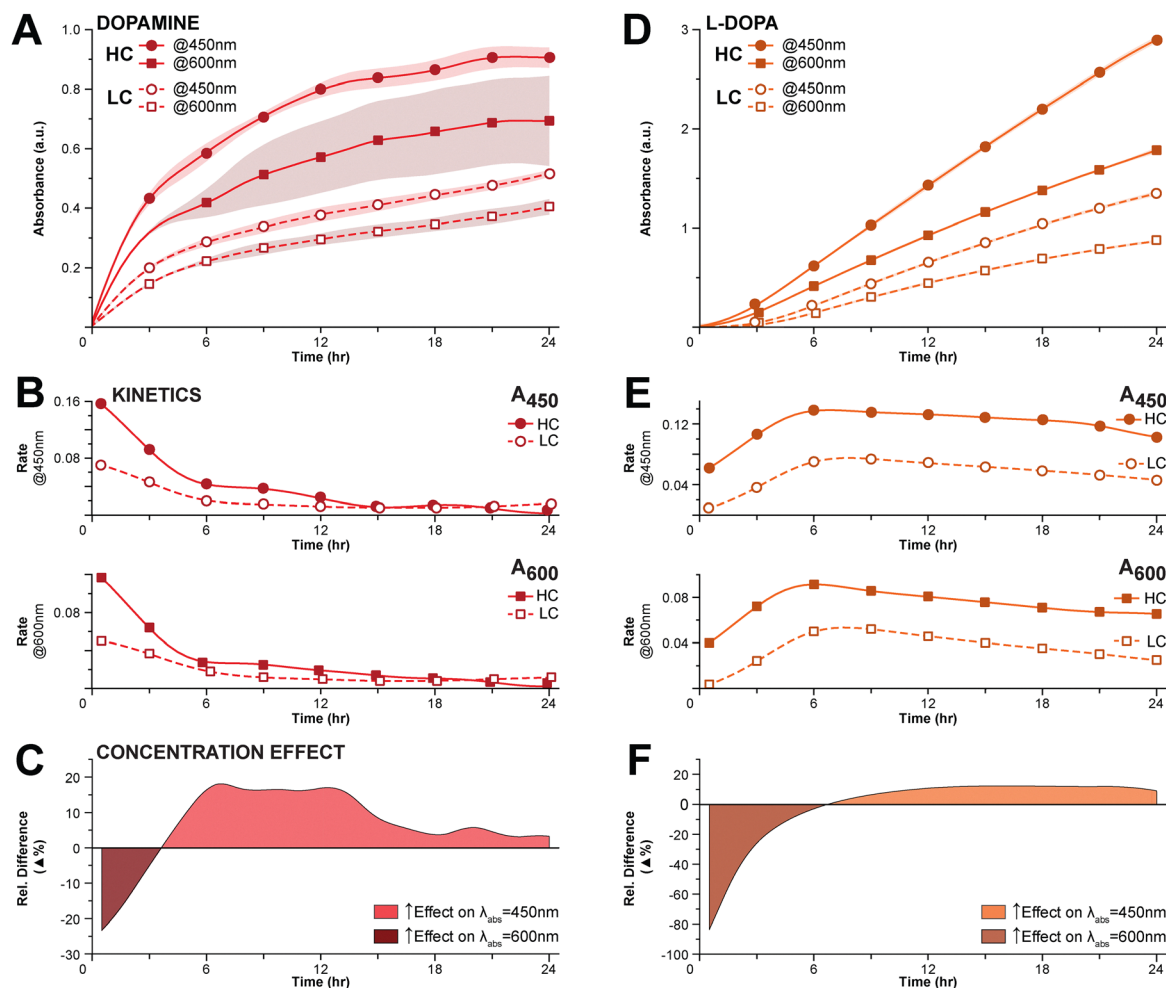


**Fig. 1** Dual-wavelength absorbance analysis and kinetics of DA and LD polymerization. Absorbance, kinetics and concentration effect data for DA (red) and LD (orange) polymerizations over 24 h. Panels A and D display absorbance data (mean  $\pm$  SD) for high-concentration (HC, 2.0 mg mL<sup>-1</sup>; filled symbols with solid lines) and low-concentration (LC, 0.5 mg mL<sup>-1</sup>; open symbols with dashed lines) conditions measured at  $A_{450}$  (circles) and  $A_{600}$  (squares). Panels B and E illustrate the rate of formation, and panels C and F show the relative difference ( $\Delta$ ) quantifying the effect of increased concentration on kinetic rates. These plots contrast the rapid, saturation-prone kinetics of DA with the delayed but sustained polymerization pathway of LD.

experimental reports.<sup>40–42</sup> In contrast,  $A_{600}$  reflects the emergence of more conjugated networks of highly polymerized eumelanin-like materials that extend the absorption spectrum to lower energies.<sup>43,44</sup> These polymer networks experience a redshift due to extensive donor-acceptor pair structures within the microstructure, which decreases the energy bandgap and enhances electron delocalization.<sup>45</sup> It is important to note that for a system that forms particles, the measured signal represents an apparent absorbance (or extinction) that includes contributions from both true chemical absorption and light scattering by the suspended aggregates. In this context, the scattering effect is expected to be more pronounced at 450 nm than at 600 nm which may exaggerate the calculated positive relative difference in the concentration effect analysis. However, as this study focuses on the comparative analysis of polymerization pathways, the overall kinetic trends and the timing of key transitions remain a valid tool for elucidating the differences between the precursor systems. Therefore, the term 'absorbance' in this context should be understood to represent

the total attenuation of light, arising from both molecular absorption by chromophores and scattering by particles.

**Poly(dopamine) (pDA) exhibits rapid, saturation-prone polymerization kinetics.** The polymerization of pDA was characterized by a sharp initial increase in absorbance for both low- (LC, 0.5 mg mL<sup>-1</sup>) and high- (HC, 2.0 mg mL<sup>-1</sup>) concentrations, which plateaued after 6 h (Fig. 1(A)).

Notably, the HC condition also exhibited significantly greater variability during this period, particularly at  $A_{600}$ , where fluctuations were more pronounced than the relatively stable progression observed under the LC condition. The kinetic rates confirm this rapid start; peak formation rates under the HC conditions occurred at the earliest measured timepoint and were substantially higher than LC at both  $A_{450}$  and  $A_{600}$ , likely driven by a reduced mean free path and increased collision frequency among reactive species at the higher concentration (Fig. 1(B)).<sup>35</sup> The eventual plateau indicates that the primary phases of chromophore formation and aggregation are largely complete, marking a transition in the dominant reaction



pathways. As will be shown later by light scattering analysis, this transition corresponds to significant changes in particle size and stability.

However, the kinetic rate decreased over time, reflecting emerging rate-limiting steps during monomer-to-polymer transitions. Both HC and LC conditions experienced a notable decline in reaction rates after the initial phase, with distinct differences in magnitude and progression. By 6 h, the kinetic rate at  $A_{450}$  had decreased substantially for both HC and LC. The rate at  $A_{600}$  under HC conditions exhibited a steeper decline compared to the more gradual decrease seen at LC. By 24 h, polymerization under HC conditions slowed down, with rates reduced by 98% at both wavelengths. In contrast, LC conditions retained approximately 22% of the peak rate, suggesting reduced aggregation and a more gradual progression.

These observed kinetic trends reflect DA's distinct electrochemical and structural properties, which enable rapid polymerization compared to other pCA precursors. In particular, DA's lower Standard Electrode Potential (SEP, 0.829 eV) compared to NE (0.851 eV) and LD (0.847 eV) reflects its reduced oxidation energy, facilitating faster electron donation.<sup>33</sup> This is further enhanced by DA's relatively low intrinsic reaction coordinate (IRC) energy (50.8 kJ mol<sup>-1</sup>), which is slightly higher than NE (49.5 kJ mol<sup>-1</sup>) but significantly lower than LD (56.5 kJ mol<sup>-1</sup>). These characteristics promote the rapid oxidation of DA to dopamine quinone (DAQ), followed by efficient cyclization into 5,6-dihydroxyindole (DHI) moieties.<sup>33</sup> These factors contribute to explain DA's faster polymerization kinetics compared to NE and LD.

The concentration effect on pDA polymerization kinetics reveals distinct temporal shifts in product formation, with differences between HC and LC conditions becoming evident over time. During the first 3 h, HC conditions exhibited a relatively higher increase in relative  $A_{600}$  signal, indicative of rapid conjugated polymer network formation (Fig. 1(C)). However, after this period, the relative difference plot became strongly positive, suggesting that the concentration effect was more pronounced for the  $A_{450}$  signal and indicating a shift toward the accumulation of oligomeric intermediates.

This interpretation is supported by analyzing the relative impact of concentration on the formation rates at the two wavelengths after the initial phase. While the absolute formation rates for both  $A_{450}$  (oligomers/intermediates) and  $A_{600}$  (conjugated polymers) decrease after peaking early under the HC condition (Fig. 1(B)), the relative effect of the higher concentration shifts over time (Fig. 1(C)). During the first 3 h, the increased concentration disproportionately accelerates the formation of conjugated networks, shown by the relatively higher increase in the  $A_{600}$  signal compared to the  $A_{450}$  signal (negative relative difference in Fig. 1(C), bottom). However, after approximately 3 h, the trend reverses; the relative difference becomes positive and exceeds 15%, indicating that the HC condition now provides a greater relative enhancement to the formation rate of  $A_{450}$ -absorbing species compared to  $A_{600}$ -absorbing ones. This suggests that while overall polymerization slows, the HC condition relatively favors the accumulation of

450 nm-absorbing species over their conversion into more complex, 600 nm-absorbing networks.

This observed shift, where the relative enhancement by a higher concentration favors  $A_{450}$ -absorbing species after 3 h, can be attributed to the evolving reaction environment. Initially rapid polymerization leads to significant aggregate formation, which likely introduces diffusion limitations that restrict the mobility of monomers and intermediates, thereby hindering their efficient incorporation into larger,  $A_{600}$ -absorbing conjugated networks. Concurrently, secondary reactions like oxidative cross-linking may further stabilize these accumulating oligomeric species ( $A_{450}$ ), impeding further growth.<sup>46</sup> As the reaction progresses towards 24 h, these concentration-dependent effects appear to lessen due to precursor depletion, leading to the stabilization of aggregates and the eventual cessation of significant polymerization activity observed as a plateau in absorbance. Ultimately, these complex dynamics underscore how precursor concentration critically modulates not only the initial speed but also the subsequent pathways and limitations of pDA polymerization.

**The carboxyl group of poly(levodopa) (pLD) induces a kinetic lag phase while promoting sustained polymerization kinetics.** pLD polymerization progresses more slowly than that of pDA. Fig. 1(D) displays the absorbance profiles over 24 h. Compared to pDA, both LC and HC conditions show a more gradual increase in absorbance during the initial hours, indicating an extended lag phase before significant polymerization occurs. Under the LC condition, the absorbance rises steadily for most of the 24 h period, only beginning to plateau slightly after 18 h. In contrast, the HC condition shows a more pronounced acceleration after the initial lag phase (~3 h) and exhibits a more sustained increase in absorbance throughout the 24 h compared to LC, suggesting a more consistent reaction rate profile.

The corresponding rates, derived from the absorbance data and plotted in Fig. 1(E), quantify this behaviour. Peak formation rates, representing the point of maximum polymerization speed, occurred later for pLD than for pDA, appearing at approximately 6 h under the HC condition and even later, around 7.5 h, under the LC condition. This confirms the delayed onset and slower initial progression observed in the absorbance curves (Fig. 1(D)).

The observed slower polymerization rates and delayed kinetics reflect the unique structural differences and resultant electrochemical properties of the LD precursor. Following the initial oxidation of LD to dopaquinone (DQ) and dopachrome (DC) under alkaline conditions, intermediates bearing the hydrophilic -COOH group likely contributed to the slower progression of polymerization by reducing the monomer's propensity for hydrophobic interactions—a critical driving force in early-stage polymerization.<sup>47,48</sup> This functional group enhances water solubility and dispersibility, favouring aqueous states over polymerized forms and delaying the onset of polymerization.<sup>10</sup> Additionally, the bulky -COOH group introduces steric hindrance, further impeding the transition from diffusion-limited to kinetically controlled polymerization, mirroring effects observed in glucose-based monomers.<sup>49</sup>



The additional  $-\text{COOH}$  functional group influences LD's structural properties and induces changes in its electrochemical behaviour, further modulating its polymerization process. LD exhibits a slightly higher DFT-calculated standard electrode potential (SEP; 0.847 eV vs. 0.829 eV for DA), reflecting a greater oxidative capacity.<sup>33</sup> However, this oxidative advantage is counterbalanced by a higher intrinsic reaction coordinate (IRC) energy for cyclization ( $56.3 \text{ kJ mol}^{-1}$ ), which imposes a substantial energetic barrier to the formation of DHI intermediates.<sup>33</sup> Additionally, the stabilization of quinone intermediates through cyclization to leucodopachrome (LDC) may have temporarily sequestered reactive species, further prolonging the lag phase.<sup>50</sup>

Monomer concentration further influenced the polymerization behaviour of pLD, particularly the duration of the lag phase and subsequent reaction kinetics (Fig. 1(E)). At LC, reduced monomer collision frequency and lower nucleation rates extended the lag phase, delaying polymerization

initiation. This delay reflects the time required to reach the critical concentrations necessary for polymerization initiation, as intermediates favour dispersion over aggregation due to the hydrophilic  $-\text{COOH}$  group.<sup>9</sup> By contrast, HC conditions appear to mitigate these effects by enhancing intermolecular interactions, overcoming solubility barriers and shortening the lag phase. Reflecting this dynamic, HC conditions exhibited an 84% higher peak rate at  $A_{450}$  and 71% at  $A_{600}$  compared to LC, highlighting the role of increased monomer availability and reactivity in driving more rapid kinetics under higher concentrations.

In contrast to the rapid, saturation-prone kinetics of pDA, pLD demonstrated a more stable polymerization profile following its delayed peak formation rate. This stability was particularly pronounced under HC conditions. For instance, after reaching its peak at  $\sim 6 \text{ h}$ , the rate for HC pLD at  $A_{450}$  and  $A_{600}$  declined by only 26% and 28%, respectively, by the 24 h endpoint. The LC condition, in contrast, exhibited a more

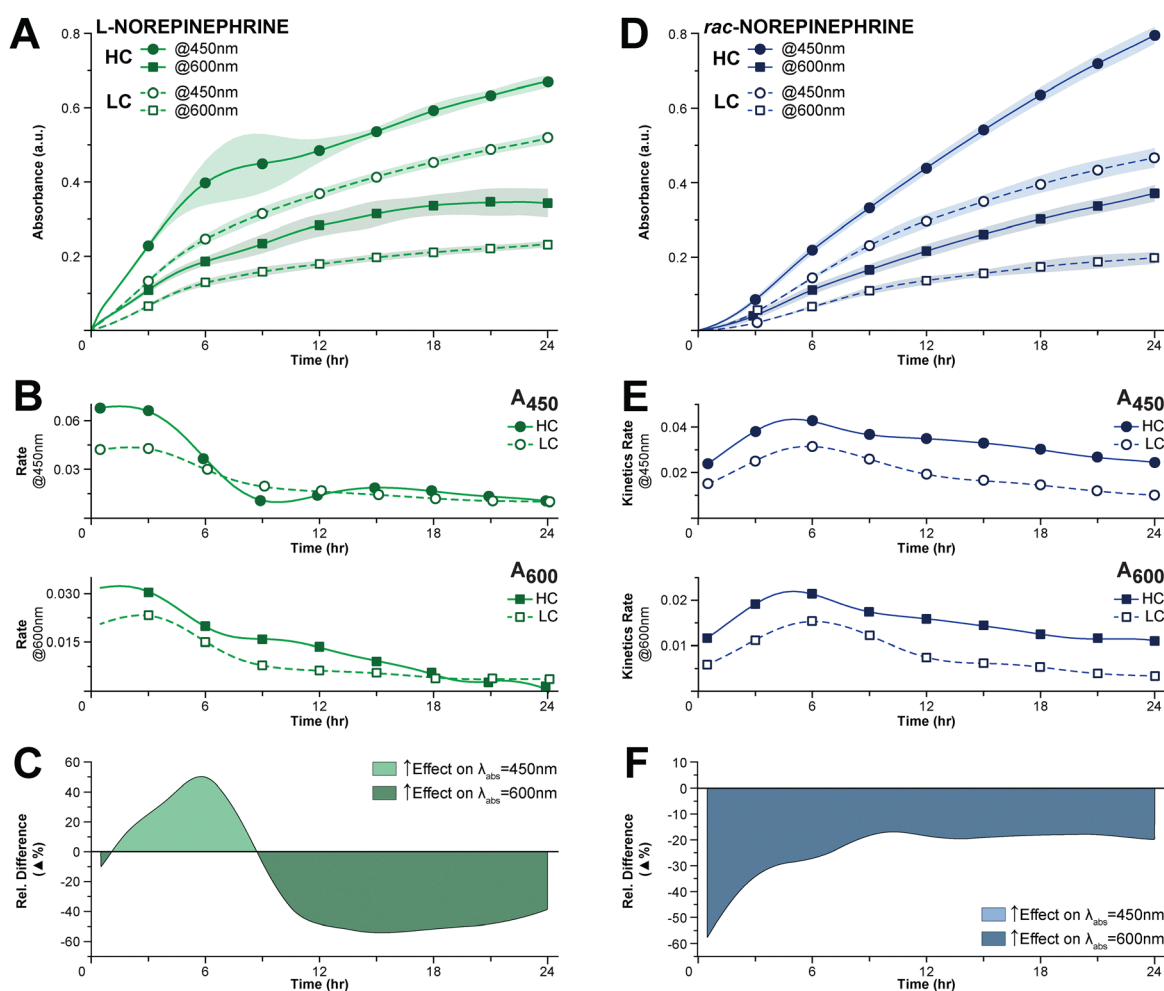


**Fig. 2** Dual-wavelength absorbance analysis and kinetics of L-NE and rac-NE polymerization. Absorbance, kinetics and concentration effect data for L-NE (green) and rac-NE (blue) polymerizations over 24 h. Panels A and D display absorbance data (mean  $\pm$  SD) for high-concentration (HC,  $2.0 \text{ mg mL}^{-1}$ ; filled symbols with solid lines) and low-concentration (LC,  $0.5 \text{ mg mL}^{-1}$ ; open symbols with dashed lines) conditions measured at  $A_{450}$  (circles) and  $A_{600}$  (squares). Panels B and E illustrate the rate of formation, and panels C and F show the relative difference ( $\Delta$ ) quantifying the effect of increased concentration on kinetic rates. These plots reveal the impact of chirality, contrasting the rapid but unstable kinetics of pLNE with the slower onset and more stable progression of pRNE.



significant decline over the same period, with its rates at  $A_{450}$  and  $A_{600}$  dropping by 38% and 54% from their peak values. This suggests that while a higher concentration of LD accelerates polymerization, its more crucial role may be in sustaining the reaction, leading to a more stable and prolonged period of polymer formation.

The relative effect of HC on  $A_{450}$  and  $A_{600}$  (Fig. 1(F)) reveals a critical transition during the first 6 h, where the concentration effect shifts from predominantly influencing  $A_{600}$  to  $A_{450}$ . This transition aligns closely with the points immediately following the respective kinetics peaks, reflecting a change in polymerization dynamics. As the formation of conjugated structures absorbing at  $A_{600}$  begins to saturate, HC conditions appear to sustain reaction rates by favouring the consistent formation of species absorbing at  $A_{450}$ . These species likely represent stabilized intermediates or early-stage oligomers that dominate the later stages of the reaction. The sustained behaviour under HC conditions is likely mediated by the structural influence of the  $-\text{COOH}$  group, which plays a dual role in moderating the polymerization process. Enhancing intermediate stability through hydrogen bonding reduces abrupt fluctuations in reaction kinetics, while its steric effects limit monomer accessibility, ensuring a more gradual and regulated progression of pLD polymerization.

**Poly(L-norepinephrine) (pLNE) polymerization exhibits pDA-like initiation but with unique kinetic instabilities.** pLNE polymerization exhibits a behaviour more closely aligned with the rapid progression of pDA than the slower, sustained polymerization of pLD, as shown by the absorbance profiles in Fig. 2(A). Under the HC condition, pronounced variability is observed, particularly in the  $A_{450}$  signal between approximately 6 and 12 h. This period of instability coincides with significant fluctuations in particle size, as will be detailed in the subsequent section, suggesting a dynamic interplay between different reaction processes occurring simultaneously. The formation and dissociation of intermediates like DHBA-NE complexes and DHBA/DHBA-quinone dimers are known to occur during NE polymerization.<sup>13</sup> Therefore, the observed fluctuations are consistent with such dynamic cycling or competition between intermediate species, leading to a less uniform progression compared to other conditions. In contrast, the LC condition exhibits a more stable and consistent progression in the absorbance signal throughout the time course. This reduced variability suggests that the processes contributing to the fluctuations (such as the rapid cycling or accumulation/dissociation of specific intermediates) may be less dominant or influential at a lower precursor concentration.

Examining the rates derived from the data (Fig. 2(B)) further clarifies the polymerization process. In HC condition, pLNE exhibits a rapid increase during the initial phase, with peak formation rates observed early, at 1.5 h for both  $A_{450}$  and  $A_{600}$ . In contrast, the LC condition shows a more gradual rise, with delayed peak reaction rates occurring at 2.5 h for  $A_{450}$  and approximately 3 h for  $A_{600}$ , reflecting a slower progression of polymerization. This delay observed specifically in the LC  $A_{600}$  kinetics, relative to  $A_{450}$  under the same condition, likely reflects the additional time required for intermediates

absorbing at 450 nm to transition into the more conjugated structures responsible for the  $A_{600}$  signal. Reduced precursor availability and consequently lower monomer collision frequency at LC further contribute to this slower progression toward higher-order polymeric species compared to HC conditions.

The peak reaction rates of pLNE reveal a concentration-dependent enhancement, with the HC condition producing a substantially higher peak rate at both  $A_{450}$  and  $A_{600}$  compared to LC. However, significant differences emerge in the decline of reaction rates following the peak. For HC conditions,  $A_{450}$  rates decline sharply between 6 and 8 h, coinciding with the period of high variability, before partially recovering. By 24 h,  $A_{450}$  rates stabilized at a level substantially below the peak. In contrast,  $A_{600}$  rates under HC conditions decline by 50% at 8 h, plateau briefly until 10 h, and then decrease to 43% of their peak by 12 h, ultimately approaching zero by 24 h. The LC condition exhibits no sharp drops, with  $A_{450}$  rates declining more gradually, while  $A_{600}$  shows a more pronounced reduction, with a 75% drop from its peak compared to 59% for  $A_{450}$ . These differences highlight the influence of precursor concentration on intermediate cycling and the formation of conjugated structures.

The polymerization behaviour of pLNE is governed by the interplay of its structural and electrochemical properties. With a SEP of 0.851 eV, DFT-based calculations indicate that NE oxidizes more slowly than DA (0.829 eV) and LD (0.847 eV), reflecting its higher oxidative threshold.<sup>33</sup> This relatively high SEP contributes to the delayed onset of oxidation and peak reaction rates, particularly when compared to DA. However, NE benefits from the lowest IRC energy (49.5 kJ mol<sup>-1</sup>) among pCA precursors, facilitating rapid cyclization and stabilization of reactive intermediates.<sup>33</sup> The  $\beta$ -hydroxyl group on the ethylamine side chain likely stabilizes intermediates *via* delocalized electron interactions, even as steric hindrance may slightly modulate reactivity.<sup>13</sup> These features underpin pLNE's polymerization, where oxidation occurs more slowly than DA, but cyclization is more efficient than LD.

Following oxidation of NE to O-quinone, tautomerization or deamination generates 3,4-dihydroxybenzaldehyde (DHBA), which can form Schiff base complexes with NE.<sup>13</sup> These DHBA-NE complexes play a significant role in early reaction dynamics, particularly under HC conditions where their formation is accelerated. Additionally, quinone species readily react to produce DHBA/DHBA-quinone dimers at a reported ratio of 1:1.<sup>13</sup> Under similar oxidative conditions, the formation of these complexes may be impaired at LC due to lower precursor availability, contributing to the slower formation of conjugated structures.

However, these dimers and complexes are unstable due to competing reactions with the abundant amine-containing NE under HC conditions, leading to dissociation into protonated DHBA units and free quinone.<sup>13</sup> The released DHBA can further react with NE *via* Schiff base formation, while the free quinone can polymerize into melanin-like structures. This dynamic cycling of intermediates—formation and dissociation of



DHBA-NE complexes and DHBA/DHBA-quinone dimers—likely introduces variability into the early reaction kinetics, mainly observed in the  $A_{450}$  signal between 6 and 12 h under HC conditions. This variability may reflect a stochastic balance between the accumulation and dissociation of reactive species alongside the progression toward conjugated structures absorbing at  $A_{600}$ . The rapid accumulation and subsequent cycling of intermediates under HC conditions may delay the transition to stable conjugated species, contrasting with the more stable progression observed under LC conditions.

The concentration effect on pLNE polymerization demonstrates distinct temporal shifts between intermediate formation and polymer growth (Fig. 2(C)). During the first 9 h, HC conditions predominantly favour the formation of species absorbing at  $A_{450}$ . This enhancement aligns with the high variability in  $A_{450}$  kinetics observed in Fig. 2(A), suggesting rapid intermediate cycling involving DHBA/DHBA-quinone dimers and Schiff base complexes with NE. During this phase, unstable dimers likely dissociate, releasing reactive intermediates that facilitate NE oxidation and promote the formation of stable conjugated polymer structures absorbing at  $A_{600}$ . This shift coincides with the resolution of variability at  $A_{450}$  and the stabilization of reaction kinetics at  $A_{600}$ , indicative of a more uniform and controlled pathway under HC conditions.

By contrast, LC conditions exhibit more gradual and less pronounced temporal shifts, reflecting slower reaction kinetics and reduced precursor availability. Limited NE concentrations hinder the rapid cycling of intermediates, resulting in reduced variability and a more extended transition period to stable polymer formation. These differences underscore the role of concentration in modulating reaction pathways, with the HC condition driving a faster and more dynamic progression compared to those observed under LC conditions.

**The chiral complexity of poly(rac-norepinephrine) (pRNE) slows polymerization onset but supports more stable kinetics.** The polymerization of pRNE exhibited unique kinetic characteristics that distinguish it from the single-enantiomer L-NE system and previously examined reactions such as DA and LD. The absorbance data (Fig. 2(D)) reveal a steady progression of polymerization under both LC and HC conditions. Unlike pLNE, which initiates its absorbance rise relatively early and quickly transitions toward higher-order conjugated structures, pRNE's early-phase growth is more gradual. Over the first 6 h, pRNE consistently lags behind pLNE in developing significant absorbance at both  $A_{450}$  and  $A_{600}$ , indicating a slower overall formation of polymeric species.

This delay becomes more apparent when examining the rates (Fig. 2(E)). While pLNE achieves its peak formation rates of polymerization products early, albeit slightly slower than DA, pRNE requires an additional 3 h to reach analogous peaks. Under the HC condition, pRNE's peak formation rate appears around 5 h at both wavelengths. However, under LC, the peak for  $A_{450}$  is approximately 6 h post-initiation, whereas the peak at  $A_{600}$  emerges roughly 0.5 h later than at  $A_{450}$ . After reaching their peak rates, the LC condition experienced a 40% decrease at 12 h and a 68% decrease by 24 h for  $A_{450}$ , while observing a

52% decrease at 12 h and a 78% decrease by 24 h for absorbance at  $A_{600}$ . In contrast, under the HC condition, there was only a 21% decrease at 12 h and a 44% decrease by 24 h for absorbance for  $A_{450}$ , alongside a 28% decrease at 12 h and a 50% decrease by 24 h for absorbance for  $A_{600}$ . This indicates that the system may need more time to form earlier stage derivatives (*e.g.*, oligomers) in conjunction with adequate precursor (*e.g.*, to create DHBA-NE complexes) before generating the fully conjugated, eumelanin-like networks that strongly absorb at longer wavelengths. This protracted timeline suggests that introducing the D-enantiomer significantly complicates the reaction pathway, extending the intermediate phases and delaying the transition into stable, conjugated states.

A possible explanation for these extended kinetics lies in the chiral complexity of the pRNE system. NE's chirality is retained in early-stage oxidation products, producing both L- and D-quinone intermediates. These chiral intermediates may interact sub-optimally with opposite enantiomers or their oligomeric derivatives, creating a more intricate and less direct polymerization landscape. Instead of rapidly funnelling intermediates into uniform oligomers and subsequently conjugated polymers, as seen in pLNE or pDA, the pRNE system manages a broader spectrum of intermediate species and partial aggregates. This multiplicity of potential pathways and reaction partners hampers the swift, efficient conversion into fully conjugated structures.

When examining the concentration effect data (Fig. 2(F)), notable differences emerge between L-NE and rac-NE systems. For pLNE, quadrupling the precursor concentration initially amplifies the formation of early-stage oligomeric and intermediate products absorbing at 450 nm, particularly within the first ~9 h, before more effectively driving the system toward conjugated, eumelanin-like structures that absorb at 600 nm. By contrast, the pRNE system responds differently to increased precursor availability. From the outset and throughout the entire 24 h period, elevated concentrations of rac-NE predominantly and consistently enhance the formation of 600 nm-absorbing species relative to those at 450 nm. This sustained emphasis on conjugated material suggests that once the racemic mixture overcomes its initial chiral and intermediate complexity, a larger precursor pool fosters a more direct or persistent pathway toward conjugated structures. The chiral complexities introduced by D-enantiomers, combined with potentially more favourable interactions at higher precursor densities (*e.g.*, between DHBA-NE complexes and various intermediate species), may help reconcile these initially sluggish kinetics into a more continuously productive route for eumelanin-like polymer formation. Thus, while L-NE relies on concentration primarily to accelerate early intermediate stages before transitioning to conjugated species, rac-NE leverages concentration to maintain a prolonged and steady formation of conjugated networks, revealing distinct mechanisms by which precursor availability and enantiomeric composition shape the polymerization landscape.

These observations suggest that both D- and L-NE enantiomers promote a more comprehensive array of initial



polymerization reactions and intermediate states, extending the window of active polymer formation and stabilization. At HC, increased monomer availability likely facilitates a more continuous and stable polymer formation process, mitigating abrupt decreases in kinetics and ensuring a smoother progression toward conjugated materials. In this sense, pRNE aligns more closely with the sustained, balanced reaction style of pLD than with the rapid, saturation-prone kinetics of pDA or the quick yet slightly delayed pattern of pLNE. Ultimately, the introduction of enantiomeric diversity transforms the kinetic landscape, showcasing how chirality and precursor composition can modulate the trajectory and final state of pCA-based materials.

### Dynamic light scattering (DLS) analysis of particle formation

Dynamic light scattering (DLS) is a key technique for measuring particle size and distribution in colloidal suspensions. Analyzing light fluctuations from particle motion reveals size distributions and helps assess how factors like precursor concentration and reaction time influence the formation of pCA NPs and  $\mu$ Ps as illustrated in Fig. 3. Particle size directly impacts the topography of deposited coatings, drug delivery efficiency, cellular internalization, and biocompatibility, making it a key parameter in designing advanced therapeutic platforms.<sup>51–55</sup>

Given the broad applications of pCAs, understanding how synthesis parameters influence particle size is critical for tailoring their properties to specific biomedical needs. Accordingly, this section focuses on the time-resolved synthesis of pCA particles conducted over 8 h, with an extended 24 h endpoint, to elucidate particle formation and growth kinetics. By examining how precursor chemistry and concentration affect particle size, this analysis provides a framework for refining the synthesis and application of pCA particles where precise size control is essential.

**pDA particle growth and heterogeneity are governed by a concentration-induced shift in aggregation.** At LC, pDA  $\mu$ Ps exhibited an initial Z-average diameter of  $316 \pm 32$  nm at 1 h, steadily increasing to a peak of  $719 \pm 107$  nm by 6 h (Fig. 3(A)). A slight non-statistically significant reduction to  $618 \pm 28$  nm was observed at 8 h, with particle size stabilizing through the 24 h measurement. This peak at 6 h correlated with the inflection point in the absorbance data, marking the onset of a plateau in the  $A_{450}$  and  $A_{600}$  signal. In contrast, pDA  $\mu$ Ps under HC conditions were statistically larger at all measured time points ( $p < 0.05$ ), with an initial Z-average diameter of  $684 \pm 26$  nm at 1 h. These particles rapidly grew to  $1604 \pm 46$  nm by 4 h, indicating the formation of large microparticle aggregates. After a transient decrease at 5 h, the size increased to  $1887 \pm 341$  nm by 8 h, remaining stable through 24 h.

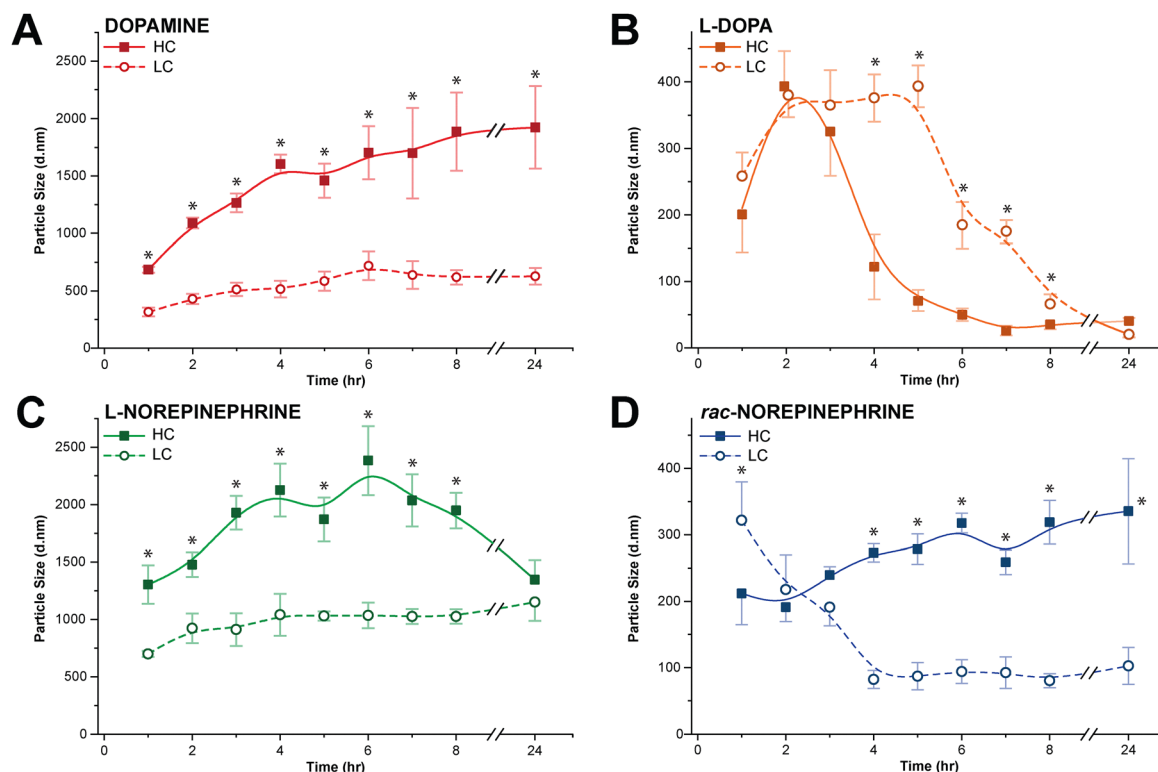


**Fig. 3** Dynamics of particle size evolution in pCA systems across precursor concentrations. Dynamic light scattering (DLS) analysis of particle size evolution for (panel A) pDA, (panel B) pLD, (panel C) pLNE, and (panel D) pRNE under high-concentration (HC,  $2.0 \text{ mg mL}^{-1}$ ; solid lines with filled squares) and low-concentration (LC,  $0.5 \text{ mg mL}^{-1}$ ; dashed lines with open circles) conditions over 24 h. Data points represent the mean particle diameter ( $d$  nm)  $\pm$  SD, with asterisks (\*) indicating statistical significance at  $p < 0.05$  (ANOVA). Particles are classified as NPs at  $\leq 100$  nm and  $\mu$ Ps at  $> 100$  nm. The analysis contrasts the formation of large, unstable microparticles by pDA and pLNE with the generation of stable nanoparticles by pLD and LC pRNE.



The pronounced size peak in Z-average diameter at 4 h under HC conditions, and the subsequent increase in standard deviation at later time points, were particularly notable. This trend, which suggests an increase in the heterogeneity of the particle population, paralleled the increased variance in the  $A_{600}$  absorbance data, particularly near the elbow of the curve. A similar, though less pronounced, pattern was observed at LC, where increased standard deviation at the 6 h size peak aligned with variability in absorbance measurements. These findings suggest concentration-dependent stages in pDA particle aggregation that contribute to heterogeneity within the particle population. Specifically, the rapid aggregation at HC appeared to drive larger initial particle sizes, followed by variability as interparticle interactions intensified during polymer growth.

Such variability likely reflects competing aggregation pathways influenced by DA's oxidative and noncovalent bonding behaviour.<sup>34,56</sup> The abundance of DA monomers and intermediates at HC likely accelerated polymerization, leading to uneven aggregation and adsorption patterns. This dynamic is supported by studies indicating that higher DA concentrations promote the formation of supramolecular structures through  $\pi$ - $\pi$  interactions and hydrogen bonding, which can destabilize particle distribution and increase heterogeneity. Conversely, LC conditions may favour slower, more uniform particle growth, as the limited availability of reactants reduces competition between aggregation pathways.

The persistence of heterogeneity at the 24 h timepoint, as reflected in both absorbance and particle size data, underscores a potential phase shift in the polymerization process. This phase may be driven by interparticle conjugation, resulting in stable but heterogeneous aggregates. The observed bimodal size distributions at HC, previously reported in related studies, suggest the coexistence of distinct aggregate populations with varying degrees of conjugation and structural stability.<sup>4,34</sup> These findings confirm that pDA aggregation involves intermediate phases of oligomer adsorption, nucleation, and growth, influenced by the balance of oxidative reactions and intermolecular interactions.

The DLS data highlight the intricate interplay between precursor concentration, aggregation behaviour, and polymerization kinetics in pDA systems. These results emphasize the importance of carefully controlling synthesis parameters to tailor particle size and distribution for specific biomedical applications (e.g., cell-instructive surfaces).

**Zwitterionic pLD forms stable NPs following an initial transient  $\mu$ P phase.** The synthesis and formation of pLD particles displayed distinct profiles compared to pDA, reflecting variations in the polymerization mechanism and stability factors driven by the zwitterionic nature of LD (Fig. 3(B)). At early time points (1–2 h), the Z-average diameter of pLD particles at both LC and HC conditions increased from an initial 200–250 nm to a transient peak of 380–393 nm. This initial stabilization phase likely corresponds to the zwitterionic balance of L-DOPA's carboxyl ( $-\text{COOH}$ ) and amino ( $-\text{NH}_2$ ) groups, which mediates solubility and aggregation kinetics.

Beyond 2 h, concentration-dependent divergence in particle size dynamics became apparent. Under HC conditions, the Z-

average diameter decreased rapidly from  $\sim 380$  nm at 2 h to  $71 \pm 15$  nm by 5 h, stabilizing at a final value of  $35 \pm 7$  nm. This dramatic reduction in the Z-average suggests a dissolution of the initial, larger microaggregates and the emergence of a stable, dominant population of nanoparticles. In contrast, LC particles exhibited delayed kinetics, maintaining sizes near 380 nm until 5 h, followed by a decline to  $66 \pm 14$  nm at 8 h and stabilization at  $20 \pm 1.3$  nm by 24 h. This size convergence at  $\sim 70$  nm across concentrations during the decline phase suggests an equilibrium governed by interparticle interactions, precursor availability, and zwitterionic charge balance.

The observed transition from transient  $\mu$ Ps to stable NPs is well-explained by the zwitterionic chemistry of the LD precursor. The  $-\text{COOH}$  group plays a critical role as its ionization state promotes electrostatic repulsion and hinders the  $\pi$ - $\pi$  stacking interactions that stabilize larger aggregates in other pCA systems, thereby favouring smaller, more homogeneous particle distributions.<sup>57,58</sup> This is supported by quaternary ammonium-assisted synthesis studies, which revealed that physical interactions, including cation- $\pi$  interactions, can modulate polymerization efficiency and particle size distribution without catalytic influences.<sup>58</sup> This chemical behaviour is reflected in the kinetics, as the DLS data aligns with the absorption profiles.

This alignment is substantiated by the complementary absorption data, which reveals a critical phase in the reaction kinetics. For HC conditions, the steep transition in the absorption profile and the peak kinetic rate at  $\sim 2$  h coincide precisely with the rapid decrease in particle size. Likewise, the slower transition for LC conditions at  $\sim 5$  h matches the more gradual particle size reduction. This indicates that the peak oxidation of the LD precursor supports nucleation events that drive polymerization and yield the final, stable nanoparticle population.

**HC drives rapid, but unstable pLNE particle growth linked to shifting polymerization kinetics.** The kinetic behaviour of pLNE particle formation resembled that of pDA but was characterized by notably larger particle sizes (Fig. 3(C)). At LC, pLNE  $\mu$ Ps exhibited an initial Z-average diameter of  $699 \pm 25$  nm at 1 h, comparable to HC pDA  $\mu$ Ps, and reached an early plateau with a Z-average diameter of  $923 \pm 130$  nm by 2 h. A modest increase to  $1040 \pm 183$  nm was observed at 4 h, followed by relative stability until 8 h and a slight rise to  $1152 \pm 163$  nm at 24 h.

Under HC conditions, pLNE  $\mu$ Ps exhibited an initial size of  $1303 \pm 167$  nm at 1 h, a value significantly larger than the LC condition ( $p < 0.05$ ). This trend of statistically larger and more variable particle sizes under HC continued for the first 8 h of polymerization, after which the particle diameter increased to  $2025 \pm 280$  nm by 4 h before entering a plateau phase. However, significant fluctuations in the Z-average diameter were observed between  $1870 \pm 190$  nm and  $2384 \pm 301$  nm from 4 h to 8 h. The large standard deviations during this period ( $\pm 10$ – $13\%$ ) reflect a highly heterogeneous and unstable particle population. Notably, this period also marked the transition point where the concentration effect shifted dominance from  $A_{450}$  to  $A_{600}$ , suggesting a shift toward forming a more conjugated polymer network at the expense of particle



size. By 24 h, the particle diameter decreased to  $1345 \pm 112$  nm, approaching the size of LC particles.

The particle sizes observed here were significantly larger than previously measured diameters of 346 nm and 130 nm for concentrations of  $1 \text{ mg mL}^{-1}$  and  $0.25 \text{ mg mL}^{-1}$ , respectively.<sup>25</sup> However, experimental differences, including the use of Tris-HCl, 2.8 mM ethanol and agitation, likely contributed to a more dispersed solution with reduced interparticle interactions, explaining the smaller particle sizes.

The observed trends suggest several mechanisms underlying the concentration-dependent stability of pLNE particles. The increased collision rate at HC likely promoted initial aggregation, resulting in larger particle sizes.<sup>34,36</sup> However, these aggregates, classified as unstable  $\mu\text{Ps}$ , appeared unstable, exhibiting size fluctuations potentially caused by repulsive forces between densely packed particles, auto-catalytic polymer decomposition, or size-related instability leading to fragmentation or re-dissolution. Conversely, LC particles reached a stable state more quickly, likely due to forming a stable core-shell structure with a dense, resistant core and a shell moderating environmental interaction.<sup>59</sup> The limited monomer availability at LC may have also restricted particle growth, resulting in a more homogeneous and stable population.

**Heterochiral interactions in pRNE lead to more stable, concentration-dependent NP and  $\mu\text{P}$  populations.** The kinetic profile of pRNE particle formation exhibited distinctive characteristics compared to the L-enantiomers, particularly in particle size and stability (Fig. 3(D)). At LC, pRNE  $\mu\text{Ps}$  had an initial Z-average diameter of  $322 \pm 58$  nm, significantly smaller than pLNE particles at the same concentration. The Z-average diameter rapidly decreased to  $82 \pm 7$  nm by 4 h, indicating a transition to a stable nanoparticle population. It remained within a narrow size range, stabilizing at approximately  $80 \pm 11$  nm at 8 h. By 24 h, a modest increase to  $103 \pm 28$  nm was observed, suggesting long-term size stabilization and minimal structural disruption.

Under HC conditions, pRNE  $\mu\text{Ps}$  displayed an initial size of  $212 \pm 47$  nm at 1 h and gradually expanded to  $308 \pm 15$  nm by 6 h. A brief phase of instability occurred between 6 and 8 h, with particle sizes fluctuating between  $267 \pm 11$  nm and  $319 \pm 33$  nm. However, unlike HC pLNE particles, pRNE  $\mu\text{Ps}$  did not experience a significant size reduction Z-average diameter after 24 h, instead maintaining a value of  $335 \pm 79$  nm. This pattern suggests that the population exhibited some heterogeneity, the underlying particle structure was considerably more robust, avoiding the large-scale collapse observed with homochiral pLNE particles.

The final size of LC pRNE particles closely aligned with the  $\sim 100$  nm reported by Liu *et al.* (2019) at 5 h, suggesting the use of rac-NE despite its lack of explicit reporting.<sup>31</sup> However, their methodology, involving higher precursor concentrations ( $2 \text{ mg mL}^{-1}$ ), elevated temperature ( $50^\circ\text{C}$ ), a more alkaline pH (NaOH in DI, pH  $\approx 11.9$ ), and agitation, likely contributed to achieving a dispersed system with uniform particle sizes. Interestingly, agitation appeared to counter aggregation in pRNE systems, contrasting with pDA systems, where agitation

typically promotes larger aggregates.<sup>18,21,60</sup> The mechanical energy provided by stirring may have played a critical role in overcoming the intrinsic aggregation tendency of rac-NE, facilitating smaller, more uniformly sized particles.

Furthermore, as previously reported, the inclusion of DHBA in DA systems may have suppressed aggregation, while HC conditions facilitated the formation of larger particles in the static environment.<sup>13,61</sup> The observed size stability of HC pRNE particles, compared to the instability of pLNE, suggests that racemic mixtures confer more potent binding energies and intermolecular forces, enhancing structural robustness. This hypothesis aligns with previous findings who demonstrated that racemic DOPA mixtures formed tightly packed crystalline heterochiral surfaces with superior mechanical stability and adhesion compared to single enantiomers.<sup>23</sup>

### Polymer dispersion ratio (PDR): a novel metric for aggregate behaviour

Understanding the dynamics of polymer aggregate formation and dispersion within various media is pivotal for advancing material design and functionality while designing the micro- and nano-topography of deposited coatings. To this end, we introduced the polymer dispersion ratio (PDR), a novel and accessible metric for elucidating the spatial distribution and temporal evolution of polymer aggregates' depositing on a substrate. PDR leverages the contrast in absorbance signals between the centre and periphery of a flat surface, providing a comprehensive view of adhesive aggregate behaviour under the influence of hydrodynamic forces, intermolecular interactions, and processing conditions. This method utilizes the horizontal motion of a standard plate reader, combined with absorbance measurements taken from the centre and two peripheral points of at the bottom of multi-well plates, effectively capturing the radial distribution of polymer aggregates across the substrate (Fig. 4(A)). The PDR is defined as the ratio of the signal detected at the centre ( $S_{\text{centre}}$ ) to the average of the signals obtained from the periphery ( $\frac{1}{n} \sum_{i=1}^n S_{\text{side},i}$ ). Fig. 4(B) illustrates a prototypical

PDR curve where distinct phases of aggregate behaviour, representing the dynamics of NP and/or  $\mu\text{P}$  populations, are marked along its path. These phases are further elaborated in Fig. 4(C), which provides a detailed description.

In the early stages of polymerization (stage A), the PDR is approximately 1, indicating a homogeneous distribution of aggregates throughout the substrate. As polymerization progresses (stage B), the PDR drops below 1, reflecting shear-induced peripheral accumulation caused by horizontal agitation of the plate reader. This agitation promotes aggregate movement toward the edges of the well as consistent shear forces act upon the system. Eventually, the aggregates approach an equilibrium distribution (stage C), with the PDR returning to approximately 1. This point is denoted as the equilibrium transition point (ETP). At later stages (stage D), the PDR rises above 1, reflecting the central accumulation of denser aggregates likely due to convection, interaggregate interactions, gravitational settling,



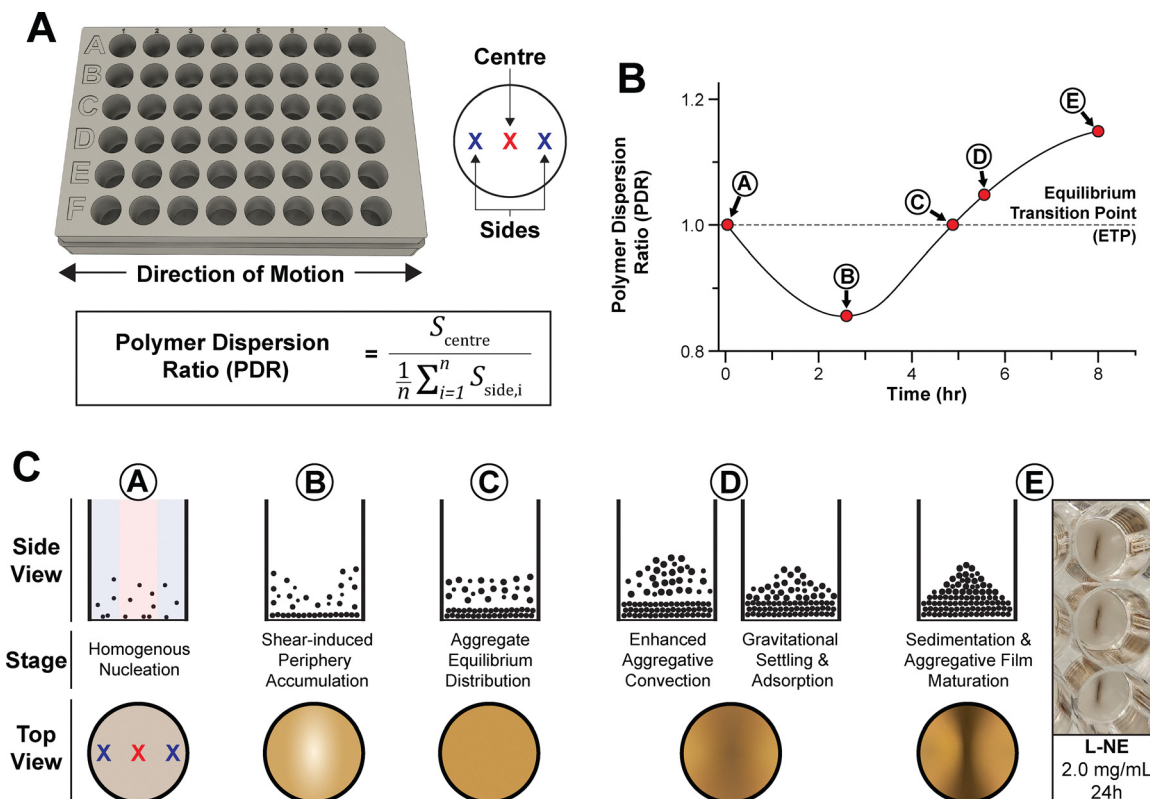


Fig. 4 Quantitative and visual framework for the polymer dispersion ratio (PDR) assay. (panel A) Schematic of a multi-well plate illustrating the locations of absorbance measurements (centre and periphery) and the formula for calculating the polymer dispersion ratio (PDR). (panel B) A prototypical curve showing the temporal evolution of PDR across distinct stages (A–E), with the equilibrium transition point (ETP) denoting the threshold where  $PDR = 1$ , representing uniform distribution. (panel C) Side and top views of each stage, illustrating the transitions from homogeneous nucleation (stage A), shear-induced periphery accumulation (stage B), aggregate equilibrium distribution (stage C), enhanced aggregative convection (stage D), to sedimentation and aggregative film maturation (stage E). A representative image of wells at 24 h for L-NE at HC ( $2.0 \text{ mg mL}^{-1}$ ) is provided, visually demonstrating the final sedimentation stage.

and adsorption phenomena. In the final stage (stage E), a continued rise in the PDR indicates sedimentation and the maturation of aggregate films at the centre of the well.

This methodology enables a deeper exploration of polymer aggregation phenomena on substrates and optimizing polymerization processes to enhance material properties. By delineating dispersion and sedimentation behaviours, PDR provides unique insights into the aggregation dynamics of pCAs and offers a potential window into substrate-specific interactions.

**The rapid aggregation kinetics of pDA are reflected in an early, concentration-dependent ETP crossing.** The PDR analysis of pDA highlighted pronounced aggregation dynamics influenced by precursor concentration and time under hydrodynamic conditions (Fig. 5(A)).

At both 450 nm and 600 nm, a higher precursor concentration accelerated the transition to central aggregate dominance. For the  $A_{450}$  signal, the HC condition crossed the equilibrium transition point (ETP) at 2.25 h, whereas the LC condition crossed approximately an hour later at 3.5 h. A similar trend was observed for the  $A_{600}$  signal, where the ETP was crossed at 2.5 h for HC and 3.0 h for LC. This demonstrates that increased concentration promotes a more rapid onset of

central accumulation, likely due to faster particle growth to a critical size ( $\sim 1100 \text{ nm}$  for HC vs.  $\sim 512 \text{ nm}$  for LC at the ETP) where gravitational and adhesive forces overcome shear-induced dispersion.<sup>34,35</sup>

Concentration also impacted the magnitude of the final sedimentation. By 24 h, the PDR values for the HC condition were substantially higher (1.96 at  $A_{450}$ ; 1.92 at  $A_{600}$ ) than for the LC condition (1.54 at  $A_{450}$ ; 1.37 at  $A_{600}$ ), and these differences were statistically significant ( $p < 0.05$ ) at both wavelengths. This indicates that the higher initial monomer concentration leads to the formation of a denser or more extensive central aggregate film over time. Post-ETP, the LC condition exhibited significant variability, particularly at  $A_{450}$ . This instability in spatial distribution coincides with the DLS data, which shows the particle population reaching its peak size and heterogeneity during this same period. In contrast, the HC condition showed a more stable increase in PDR after 4 h, correlating with the stabilization of its larger particle population ( $\sim 1604 \text{ nm}$ ). These dynamics underscore how precursor concentration critically modulates both the temporal evolution and the final spatial distribution of pDA aggregates.

**pLD resists central sedimentation and maintains a stably dispersed profile across concentration conditions.** PDR measurements for pLD revealed consistent behaviour across



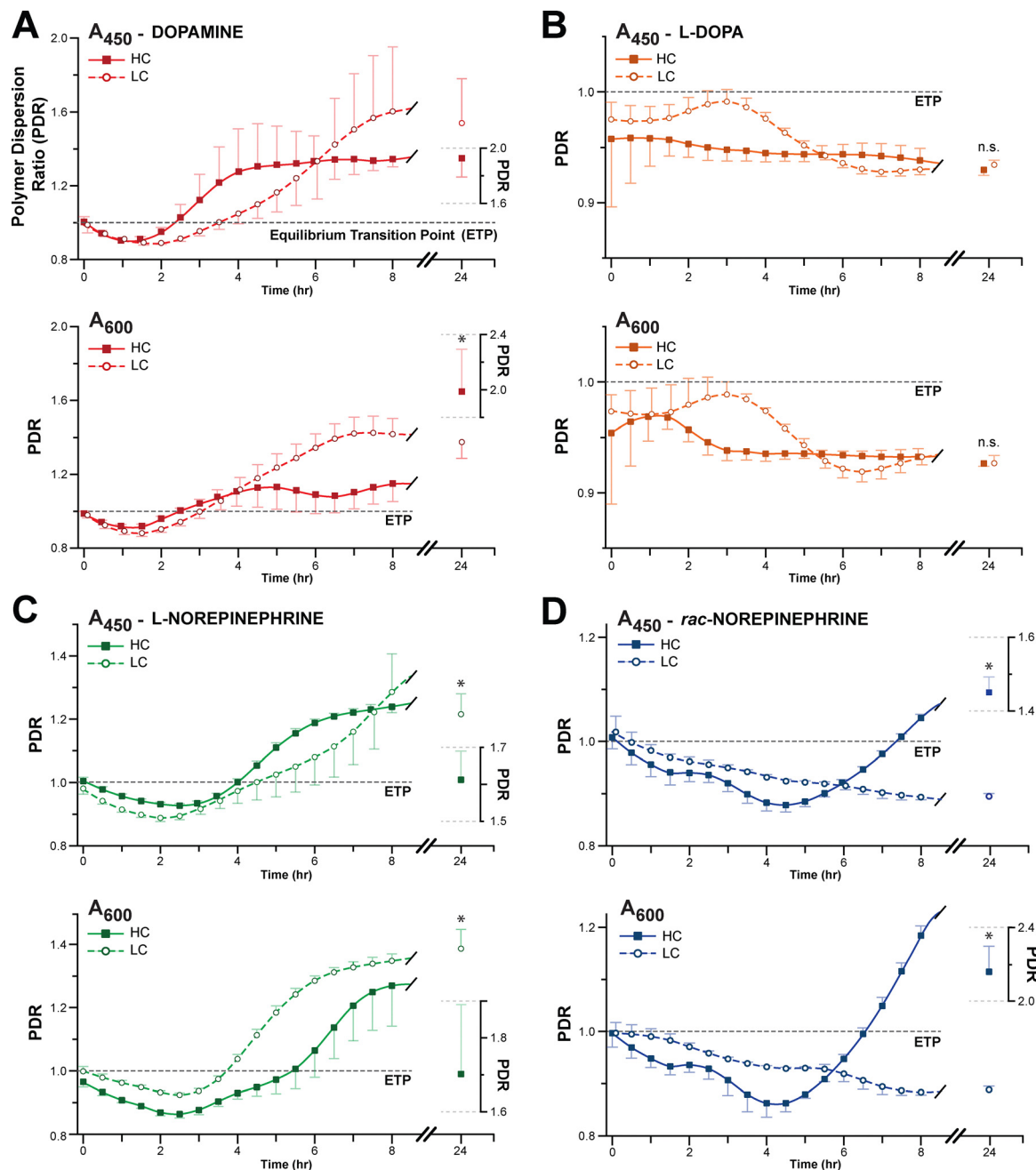


**Fig. 5** Time-resolved polymer dispersion ratio (PDR) at dual wavelengths. Time-resolved PDR profiles for (panel A) pDA, (panel B) pLD, (panel C) pLNE, and (panel D) pRNE. Within each panel, subplots are organized by wavelength ( $A_{450}$ , top;  $A_{600}$ , bottom) to compare high-concentration (HC,  $2.0 \text{ mg mL}^{-1}$ ; solid lines with filled squares) and low-concentration (LC,  $0.5 \text{ mg mL}^{-1}$ ; dashed lines with open circles) conditions over 24 h. Measurements represent the mean  $\pm$  SD, with asterisks (\*) indicating statistical significance at  $p < 0.05$  (ANOVA). The equilibrium transition point (ETP) indicates the threshold where PDR transitions from peripheral accumulation ( $\text{PDR} < 1$ ) to central aggregate dominance ( $\text{PDR} > 1$ ). The PDR profiles reveal a diverse range of aggregation behaviours, from the rapid central accumulation of pDA and the stable dispersion of pLD to the concentration-gated switch observed for pRNE.

wavelengths, indicative of a uniform response to hydrodynamic forces during the polymerization process (Fig. 5(B)). Unlike the aggregation-prone dynamics observed in pDA, pLD exhibited a predominantly non-aggregative nature, characterized by homogeneous particle dispersion. This behaviour was consistent with its molecular structure, where the carboxyl ( $-\text{COOH}$ ) group on the  $\beta$ -carbon of LD imparts hydrophilic and

electrostatic stabilization that favour dispersion over sustained aggregation.

Across both wavelengths and concentrations, PDR for pLD remained below the ETP for 24 h, confirming a dispersion-favouring regime that resists centre-weighted sedimentation. At HC a shallow transient maximum appears at  $\sim 1 \text{ h}$ , while at LC the corresponding feature occurs later ( $\sim 3 \text{ h}$ ) and rises closer



to ETP before declining toward a shared steady state ( $\approx 0.93$ – $0.94$  by 24 h). This timing mirrors DLS, where the PDR humps precede a collapse in Z-average diameter (HC:  $\sim 3$ – $4$  h; LC:  $\sim 5$ – $6$  h), consistent with a short mesoscale-cluster window that is depleted by fragmentation and/or surface deposition.

LC approaches ETP more closely than HC at both wavelengths, indicating that the LC system briefly attains a more uniform particle distribution (*i.e.*, a nearly homogeneous projection in the PDR sampling plane) before declining toward the shared steady state. By contrast, the HC system remains distinctly edge-weighted throughout, likely due to a higher number density of highly charged nascent particles; mutual repulsion and ongoing nucleation maintain dispersion weighting.

Notably, the  $A_{450}$  maximum is more muted than  $A_{600}$  at HC. Because apparent absorbance includes scattering, and scattering is stronger at shorter wavelengths, we emphasize within-wavelength LC  $\leftrightarrow$  HC comparisons; the qualitative hump asymmetry is compatible with complex scattering at 450 nm becoming more prominent at higher particle densities.

This transient PDR peak is correlated with the particle size evolution measured by DLS. The PDR hump in both LC ( $\sim 3$  h) and HC ( $\sim 1$  h) precedes a subsequent collapse in the Z-average diameter observed in DLS (LC:  $\sim 5$ – $6$  h; HC:  $\sim 3$ – $4$  h). This suggests a brief mesoscale-cluster window where transient aggregates form, reach a peak state of near-homogeneity (for LC), and are then depleted from the solution, likely through a combination of fragmentation and surface deposition.

Following this transient window, the systems settle. By approximately 4 h for HC and 8 h for LC, the PDR values stabilize to similar levels ( $\approx 0.93$ – $0.94$ ) that are maintained through 24 h. This demonstrates that the stabilizing effect of the  $-\text{COOH}$  group is the dominant factor governing the spatial distribution of pLD aggregates. This intrinsic property is not overcome even by a four-fold increase in precursor concentration, highlighting the distinctive nature of pLD polymerization. This behaviour makes pLD particularly suitable for applications requiring highly stable and uniformly dispersed particles, such as biosensors or drug delivery.

**pLNE exhibits a complex, concentration-dependent aggregation profile with faster stabilization at LC.** The aggregation profile of pLNE revealed a complex, concentration-dependent behaviour where LC paradoxically led to a more rapid stabilization of the central aggregate (Fig. 5(C)).

At both wavelengths, the LC condition crossed the equilibrium transition point (ETP) and reached a stable state of central aggregation faster than the HC condition. For the  $A_{450}$  signal, the ETP was crossed at  $\sim 3.5$  h for LC *versus*  $\sim 4.5$  h for HC. A similar trend was observed for the  $A_{600}$  signal, with the ETP crossed at  $\sim 4.0$  h for LC *versus*  $\sim 5.5$  h for HC. This suggests that the abundance of monomers under HC conditions may facilitate prolonged, secondary aggregation events that delay the formation of a stable central population. In contrast, the limited monomer availability at LC may promote a more direct pathway to a stable, centrally aggregated state. This interpretation is strongly supported by the DLS, which shows that the HC condition produces larger but significantly

more unstable aggregates that undergo substantial size fluctuations, whereas the LC aggregates reach a stable size more rapidly.

While the LC condition stabilized more quickly, the HC condition ultimately resulted in a greater degree of central sedimentation. By 24 h, the PDR values for the HC condition ( $\sim 1.65$  at  $A_{450}$ ;  $\sim 1.69$  at  $A_{600}$ ) were significantly higher than for the LC condition ( $\sim 1.21$  at  $A_{450}$ ;  $\sim 1.39$  at  $A_{600}$ ), and these differences were statistically significant ( $p < 0.05$ ) at both wavelengths. Interestingly, under HC conditions, the PDR values for both wavelengths converged to a similarly high value. This suggests a consistent aggregation mechanism dominated by a similar population of conjugated species, potentially involving the formation of DHBA-NE complexes which are known to drive polymerization dynamics in pNE systems.<sup>13</sup> This behaviour highlights the sensitivity of pLNE aggregation to precursor concentration, where LC conditions favour rapid stabilization, while HC conditions promote more extensive, albeit delayed, central accumulation.

**pRNE demonstrates a concentration-gated switch between pLD-like dispersion and pDA-like aggregation.** The aggregation behaviour of pRNE exhibits a concentration-gated switch, behaving pLD-like (dispersed) at LC and pDA/pLNE-like (centrally aggregating) at HC, suggesting that chirality-enabled interparticle adhesion emerges only once a critical precursor density is reached (Fig. 5(D)).

Under LC conditions, pRNE behaved similarly to pLD, exhibiting a dispersed profile characterized by the formation of small, stable nanoparticles with a Z-average diameter that plateaued at approximately 102 nm. Correspondingly, at both  $A_{450}$  and  $A_{600}$ , the PDR remained consistently below the ETP for the entire 24 h period, stabilizing at a final value of  $\sim 0.94$ . This suggests that at low concentrations, the chiral complexity of the racemic mixture may hinder efficient, ordered aggregation, favouring a more stable and uniform particle dispersion.

In stark contrast, the HC condition triggered a dramatic shift to a centrally aggregating system. At  $A_{600}$ , the PDR crossed the ETP at  $\sim 6.5$  h, followed by  $A_{450}$  at  $\sim 7.5$  h. After crossing the ETP, the PDR values rose to final values of 2.17 ( $A_{600}$ ) and 1.52 ( $A_{450}$ ). Compared to the dispersed LC condition (PDR  $\approx 0.94$ ), these final PDR values for the aggregated HC state represent a statistically significant difference ( $p < 0.05$ ) at both wavelengths. Notably, this transition to central dominance between  $\sim 6.5$  and  $\sim 7.5$  h coincides with a period of particle-size instability observed *via* DLS, likely reflecting dynamic adsorption and restructuring of aggregates at the well centre as they begin to form a film. This demonstrates that a higher concentration is required to overcome the initial kinetic barriers imposed by the racemic mixture, enabling strong interparticle forces that drive dense central aggregation.

Despite pRNE aggregates under HC conditions having a Z-average diameter approximately  $\sim 75\%$  smaller than pLNE aggregates, they show  $\sim 28\%$  higher central accumulation. This observation strongly suggests that the racemic composition enhances interparticle adhesion and aggregate density. Such behaviour is consistent with heterochiral interactions in



racemic systems that can promote tighter packing and superior mechanical stability, but only once a critical concentration of interacting species is reached.<sup>23</sup> Together, these data highlight the unique role of chirality in modulating pCA self-assembly. The data suggest that the aggregation is triggered by concentration-dependent interparticle forces rather than continued particle growth, offering a practical mechanism to control aggregate behaviour by adjusting the initial precursor concentration.

## Conclusion

This study comprehensively examined the polymerization behaviour of four pCA polymerization systems—pDA, pLD, pLNE, and pRNE—under controlled precursor concentration and chirality conditions. By integrating dual-wavelength absorbance measurements, kinetic rate analysis, DLS data, and the novel polymer dispersion ratio (PDR), we established associations between molecular structure, polymerization pathways, and resulting material properties. By combining these complementary techniques, we gained a mechanistic understanding of how each parameter (chemistry, concentration, chirality) can be leveraged to tailor material outcomes, thereby advancing rational biomaterial design precisely.

Each precursor demonstrated a distinctive temporal profile from the absorption and kinetics perspective. pDA exhibited rapid initial polymerization with early saturation, reflecting its favourable electrochemical parameters, while pLD's slower kinetics and extended lag phase underscored the stabilizing influence of its  $-\text{COOH}$  group. The addition of a chiral  $-\text{OH}$  group in pLNE produced a hybrid profile, initially resembling pDA's rapid formation but showing intermediate cycling and delayed transitions under high-concentration conditions. In contrast, the mixed enantiomeric profile of pRNE introduced chiral complexity, delaying polymerization peaks yet ultimately achieving more sustained formation of conjugated species at higher concentrations. These observations highlight how subtle differences in precursor functional groups, chiral centres, and concentration levels can yield remarkably varied kinetic landscapes. These provide a strategic framework for selecting precursors and conditions to achieve desired kinetic outcomes.

DLS measurements provided further insight into particle formation and growth. pDA and pLNE tended toward larger  $\mu\text{Ps}$  ( $>100\text{ nm}$ ) and exhibited more pronounced size fluctuations under HC, while pLD's zwitterionic nature favoured the formation of stable NPs ( $\leq 100\text{ nm}$ ) following a transient  $\mu\text{P}$  phase. The racemic pRNE system, in turn, demonstrated enhanced structural robustness at elevated concentrations, yielding smaller and more stable particles than its L-enantiomer counterpart. These size evolution patterns directly relate to each precursor's polymerization pathway, with intermediate stabilization, steric effects, and electrostatic interactions all shaping NP and  $\mu\text{P}$  assemblies. Crucially, previous work has established that cells interact directly with the aggregates formed during pDA deposition.<sup>21</sup> Therefore, understanding and controlling particle size and aggregation, as

detailed in this study, is essential for designing pCA materials intended for cell-instructive and/or antibacterial surfaces. Such particle-level control is thus essential for biomedical applications, from drug delivery and imaging to regenerative medicine and functional coatings, where precise particle dimensions and colloidal stability can improve performance and safety. For example, our findings provide a clear design strategy: to generate small, stable NPs for drug delivery, a researcher should select LC pRNE. If the functionality of hydrophilic carboxyl groups is also required (e.g., for bioconjugation), pLD is the optimal choice. In either case, the temporal evolution of particle size must be considered to isolate the desired population. Conversely, to create a micro-topographical coating for cell-instructive or antibacterial surfaces, a researcher should use HC pDA or pLNE to generate the necessary larger aggregates ( $>1\text{ }\mu\text{m}$ ).

The PDR introduced in this study offered a novel window into the spatial and temporal aggregation dynamics of these pCA systems. By quantifying absorbance differences between the well centre and periphery, PDR tracked the evolution from homogeneous dispersion to peripheral clustering, equilibrium, and eventual central aggregation or sedimentation. This metric revealed distinct patterns: pDA formed dense central aggregates, pLD remained well-dispersed, while pLNE and pRNE showed complex states balancing peripheral and central accumulation. Crucially, the ability of PDR to monitor these aggregation dynamics provides valuable information for optimizing coating processes where aggregate distribution influences cellular response. Complementing kinetics and DLS data, PDR links macroscopic aggregation patterns to underlying molecular and colloidal processes, demonstrating its utility as a versatile tool for studying aggregation in pCA and other polymeric/colloidal systems. From a practical standpoint, these distinct aggregation patterns can be leveraged to engineer specific surface properties. For example, the highly dispersed nature of pLD is ideal for creating uniform films. Notably, while both pDA and pLNE are aggregative, particularly at HC, pRNE offers a unique, concentration-switchable behaviour: at LC, it remains dispersed, suitable for homogeneous coatings, while at HC, it becomes strongly aggregative, thereby providing a pathway to create adhesive, patterned surfaces from the same precursor chemistry. This ability to tune the final material outcome, from dispersed to aggregated, simply by adjusting concentration represents a powerful tool for rational biomaterial design.

These findings demonstrate that adjusting precursor chemistry, concentration, and chirality allows for deliberate tuning of polymerization kinetics, particle size distributions, and aggregate organization in pCA-based systems. By leveraging the insights gained from multi-wavelength absorbance measurements, detailed kinetic analyses, DLS-based particle characterization, and the innovative PDR metric, researchers can more confidently engineer pCA materials with properties optimized for specific biomedical and technological applications, particularly those involving direct cell-material interactions. This work lays a foundation for future investigations exploring additional enantiomeric ratios, reaction conditions,



and application-specific functionalization. A critical next step will be to elucidate the underlying molecular mechanisms, including the reaction energetics of intermediate formation and the inter-oligomer binding energies that drive particle assembly, for which DFT modelling would be invaluable. These simulations could then be correlated with direct morphological (*e.g.*, SEM), spectroscopic (*e.g.*, EPR, ATR-FTIR), and electrochemical (*e.g.*, cyclic voltammetry) characterization of the materials, which will require overcoming the inherent technical challenges associated with analyzing such diverse particle populations and thin adhesive films. While this study focuses on the foundational role of precursor chirality, it is plausible that these initial conditions also influence higher-order chiral structures, such as the final conformation of the polymer chains themselves; investigating this link, potentially through techniques such as circular dichroism spectroscopy or X-ray scattering as has been demonstrated for poly(DOPA),<sup>23</sup> represents an important avenue for future research.

Ultimately, this work paves the way toward increasingly sophisticated and customizable pCA-based biomaterials designed not only for advanced therapeutic, diagnostic, and tissue engineering platforms but also for broader uses where pDA has already demonstrated significant impact, such as in stimuli-responsive smart materials,<sup>62</sup> functional hydrogels,<sup>63</sup> energy storage, environmental remediation, and functional surface engineering,<sup>46</sup> further extending the reach and utility of these versatile materials. The distinct behaviours observed between the homochiral L-NE and racemic NE systems also suggest exciting opportunities to create novel materials with unique, intermediate properties by utilizing targeted enantiomeric blends.

## Materials and methods

### Chemicals

Dopamine hydrochloride (DA; Sigma Aldrich, USA), L-norepinephrine hydrochloride (L-NE; Sigma Aldrich, USA), DL-norepinephrine hydrochloride (rac-NE; VWR, USA), and L-3,4-dihydroxyphenylalanine (LD; Fisher Scientific, USA) were used as received. Tris(hydroxymethyl)aminomethane hydrochloride (Tris-HCl; Sigma Aldrich, USA, Cat# T5941) was used to prepare the buffer solution.

### Preparation

Precursor stock solutions were prepared by dissolving DA, LD, L-NE, or rac-NE in 10 mM Tris-HCl buffer (pH 8.6) to final concentrations of 0.5 mg mL<sup>-1</sup> (low concentration, LC) and 2.0 mg mL<sup>-1</sup> (high concentration, HC). Solutions were vortexed until visually clear, ensuring complete dissolution of the precursor. Due to significantly longer dissolution times required for LD compared to the other precursors, LD solutions were always prepared first when handling multiple precursors concurrently, followed by rac-NE, L-NE, and finally DA, reflecting their relative dissolution rates. 0.5 mL of the prepared precursor solution was aliquoted into each well of a 48-well

polystyrene plate (non-tissue culture treated; Cellstar PS, Greiner Bio-One, Germany, Ref# 677102) and the plate was immediately placed into the microplate reader.

### Absorbance measurements

Measurements were performed using a Tecan Infinite 200 Pro microplate reader at 450 nm ( $\Delta\lambda = \pm 10$  nm;  $A_{450}$ ) and 600 nm ( $\Delta\lambda = \pm 10$  nm;  $A_{600}$ ). These measurements were conducted on samples from three independent experiments ( $n = 3$ ), with each experimental condition represented by three wells per experiment. Readings were taken every 30 min in a  $3 \times 3$  grid over the 24 h period while the plate remained inside the reader, which was pre-warmed for at least 1 h prior to measurements and maintained a temperature range of  $21 \pm 1$  °C throughout the experiment. Kinetic absorbance data was derived by averaging measurements from two peripheral ('side') points (positions [0,1] and [2,1], 2.8 mm from the centre [1,1]) within the  $3 \times 3$  grid scan of each well. The kinetic rate was calculated as the slope of these average absorbance curves with respect to time.

### Relative concentration effect calculation

To assess the differential impact of increasing precursor concentration on the kinetics measured at  $A_{450}$  versus  $A_{600}$ , the relative difference ( $\Delta$ ) was calculated over time. This metric compares the ratio of HC to LC kinetic rates at each wavelength using the equation:  $\Delta = (k_{450}^{\text{HC}}/k_{450}^{\text{LC}}) - (k_{600}^{\text{HC}}/k_{600}^{\text{LC}})$ . A key advantage of this ratiometric calculation is its function as an internal control. Comparing the ratios of the kinetic rates effectively normalizes for systemic variables, thereby isolating the specific, wavelength-dependent impact of precursor concentration on the formation of early-stage intermediates versus more conjugated polymer networks. Therefore, a positive  $\Delta$  value indicates that the four-fold increase in concentration had a proportionally greater accelerating effect on the kinetics measured at 450 nm compared to 600 nm, whereas a negative value signifies a proportionally greater effect on the kinetics measured at 600 nm.

### Polymer dispersion ratio (PDR)

The PDR was calculated using absorbance measurements obtained concurrently with the kinetic data, employing the same instrument settings and 48-well plates. For each well, in a  $3 \times 3$  grid scan, the PDR was calculated from the absorbance measured at the centre ( $S_{\text{centre}}$ , position [1,1]) and two peripheral locations along the axis of plate reader movement ( $S_{\text{side}}$ , positions [0,1] and [2,1]) using the formula shown in Fig. 4(A). The equilibrium transition point (ETP) is defined as the time point where PDR = 1, representing an even absorbance signal distribution across the measured points in the well.

### Dynamic light scattering (DLS)

Particle hydrodynamic diameter (Z-average diameter,  $d$  nm) and size distributions were measured using a Zetasizer Nano ZS instrument (Malvern Instruments, UK) equipped with a He-Ne laser (633 nm) and operating at a backscatter angle of 173°.



Measurements were conducted at 25 °C in disposable polystyrene cuvettes (Sarstedt, Ref# 67.742). Data was analyzed using Malvern Zetasizer software v8.02 using the Cumulants analysis model. As pCA suspensions are inherently polydisperse, the Z-average diameter is presented here as a metric to track the temporal evolution of the dominant particle size rather than as a measure of a monodisperse population. In this study, particles  $\leq 100$  nm in diameter are referred to as nanoparticles (NP), while particles  $> 100$  nm are referred to as microparticles ( $\mu$ P). For DLS analysis, samples derived from each of the three experiments ( $n = 3$ ) were dispersed in 10 mM Tris-HCl buffer (pH 8.6) and vortexed briefly prior to measurement to homogenize the suspension with the final dispersion volumes standardized to 1 mL for measurement.

### Statistical analysis

To compare the effect of precursor concentration (LC vs. HC) within each precursor system at given time points, data sets were analysed using two-way ANOVA. Tukey's HSD *post hoc* test was applied when multiple mean comparisons were required. Statistical significance was defined as  $p < 0.05$ . Results are reported as mean  $\pm$  SD, and statistically significant differences are indicated by asterisks (\*) in the figure panels. All statistical analyses were performed using GraphPad Prism 8 (GraphPad Software, Inc.) and OriginPro.

### Author contributions

A. J. S.: conceptualization, methodology, investigation, formal analysis, writing – original draft. F. V.: supervision, funding acquisition, writing – review & editing.

### Conflicts of interest

The authors declare no conflict of interest.

### Data availability

The data that support the findings of this study are openly available in Zenodo at <https://doi.org/10.5281/zenodo.17082180>. This dataset includes time-resolved absorbance, kinetic rate, dynamic light scattering (particle size), and Polymer Dispersion Ratio (PDR) data.

### Acknowledgements

This work was supported by the Natural Sciences and Engineering Research Council of Canada (NSERC) through the Discovery grant, by the Canada Foundation for Innovation (CFI), and the Ontario Ministry of Research and Innovation (MRI) through the Leaders of Opportunity (LOF) fund. AS acknowledges financial support from the Natural Sciences and Engineering Research Council (NSERC) through the Postgraduate Scholarship – Doctoral (PGS-D) program, as well as the Ontario Graduate Scholarship (OGS) program through the Queen Elizabeth II Graduate

Scholarship in Science and Technology (QEII-GSST). The authors thank Dr Xudong Cao and Yingshu Leng at the University of Ottawa for their assistance with the DLS.

### References

- 1 H. Lee, S. M. Dellatore, W. M. Miller and P. B. Messersmith, *Science*, 2007, **318**, 426–430.
- 2 C. Zhang, L. Gong, L. Xiang, Y. Du, W. Hu, H. Zeng and Z. K. Xu, *ACS Appl. Mater. Interfaces*, 2017, **9**, 30943–30950.
- 3 H. A. Lee, Y. Ma, F. Zhou, S. Hong and H. Lee, *Acc. Chem. Res.*, 2019, **52**, 704–713.
- 4 H. Hemmatpour, O. De Luca, D. Crestani, M. C. A. Stuart, A. Lasorsa, P. C. A. van der Wel, K. Loos, T. Giousis, V. Haddadi-Asl and P. Rudolf, *Nat. Commun.*, 2023, **14**, 664.
- 5 Y. Fu, L. Yang, J. Zhang, J. Hu, G. Duan, X. Liu, Y. Li and Z. Gu, *Mater. Horiz.*, 2021, **8**, 1618–1633.
- 6 L. Jia, F. Han, H. Wang, C. Zhu, Q. Guo, J. Li, Z. Zhao, Q. Zhang, X. Zhu and B. Li, *J. Orthop. Translat.*, 2019, **17**, 82–95.
- 7 M. Godoy-Gallardo, N. Portoles-Gil, A. M. Lopez-Periago, C. Domingo and L. Hosta-Rigau, *Mater. Sci. Eng., C*, 2020, **117**, 111245.
- 8 A. Jin, Y. Wang, K. Lin and L. Jiang, *Bioact. Mater.*, 2020, **5**, 522–541.
- 9 X. Tan, P. Gao, Y. Li, P. Qi, J. Liu, R. Shen, L. Wang, N. Huang, K. Xiong, W. Tian and Q. Tu, *Bioact. Mater.*, 2021, **6**, 285–296.
- 10 A. Michalicha, A. Roguska, A. Przekora, B. Budzynska and A. Belcarz, *Carbohydr. Polym.*, 2021, **272**, 118485.
- 11 J. Ghodsi and A. A. Rafati, *Anal. Bioanal. Chem.*, 2018, **410**, 7621–7633.
- 12 H. Guo, Y. Sun, X. Niu, N. Wei, C. Pan, G. Wang, H. Zhang, H. Chen, T. Yi and X. Chen, *J. Chromatogr. A*, 2018, **1578**, 91–98.
- 13 S. Hong, J. Kim, Y. S. Na, J. Park, S. Kim, K. Singha, G. I. Im, D. K. Han, W. J. Kim and H. Lee, *Angew. Chem., Int. Ed.*, 2013, **52**, 9187–9191.
- 14 M. Park, M. Shin, E. Kim, S. Lee, K. I. Park, H. Lee, J.-H. Jang and J. Wang, *J. Nanomater.*, 2014, **2014**, 1–10.
- 15 M. B. Taskin, R. Xu, H. Zhao, X. Wang, M. Dong, F. Besenbacher and M. Chen, *Phys. Chem. Chem. Phys.*, 2015, **17**, 9446–9453.
- 16 S. M. Kang, J. Rho, I. S. Choi, P. B. Messersmith and H. Lee, *J. Am. Chem. Soc.*, 2009, **131**, 13224–13225.
- 17 Z. Xu, T. Wang and J. Liu, *Int. J. Mol. Sci.*, 2022, **23**, 7278.
- 18 L. Su, Y. Yu, Y. Zhao, F. Liang and X. Zhang, *Sci. Rep.*, 2016, **6**, 24420.
- 19 L. Dou, X. Wang, Y. Bai, Q. Li, L. Luo, W. Yu, Z. Wang, K. Wen and J. Shen, *Int. J. Biol. Macromol.*, 2024, **282**, 136762.
- 20 T. S. Sileika, H. D. Kim, P. Maniak and P. B. Messersmith, *ACS Appl. Mater. Interfaces*, 2011, **3**, 4602–4610.
- 21 A. J. Steeves and F. Variola, *J. Mater. Chem. B*, 2020, **8**, 199–215.



- 22 P. Chen, S. He, T. Wang, C. Wang, J. Tao and Y. Li, *Nat. Commun.*, 2025, **16**, 7127.
- 23 Y. Shen, R. Su, D. Hao, X. Xu, M. Reches, J. Min, H. Chang, T. Yu, Q. Li, X. Zhang, Y. Wang, Y. Wang and W. Qi, *Nat. Commun.*, 2023, **14**, 3054.
- 24 Z. Lu, S. Acter, B. M. Teo and R. F. Tabor, *J. Mater. Chem. B*, 2021, **9**, 9575–9582.
- 25 Z. Lu, A. M. Douek, A. M. Rozario, R. F. Tabor, J. Kaslin, B. Follink and B. M. Teo, *J. Mater. Chem. B*, 2020, **8**, 961–968.
- 26 Z. Lu, A. J. Quek, S. P. Meaney, R. F. Tabor, B. Follink and B. M. Teo, *ACS Appl. Bio Mater.*, 2020, **3**, 5880–5886.
- 27 V. Baldoneschi, P. Palladino, M. Banchini, M. Minunni and S. Scarano, *Biosens. Bioelectron.*, 2020, **157**, 112161.
- 28 S. M. Kang and H. Lee, *Bull. Korean Chem. Soc.*, 2013, **34**, 960–962.
- 29 Y. Liu, X. Nan, W. Shi, X. Liu, Z. He, Y. Sun and D. Ge, *RSC Adv.*, 2019, **9**, 16439–16446.
- 30 R. P. Liang, C. Y. Xiang, J. W. Wang and J. D. Qiu, *J. Chromatogr. A*, 2013, **1284**, 194–201.
- 31 X. Liu, Z. Xie, W. Shi, Z. He, Y. Liu, H. Su, Y. Sun and D. Ge, *ACS Appl. Mater. Interfaces*, 2019, **11**, 19763–19773.
- 32 D. Yang, X. Wang, Q. Ai, J. Shi and Z. Jiang, *RSC Adv.*, 2015, **5**, 42461–42467.
- 33 C. Zhang, L. Xiang, J. Zhang, C. Liu, Z. Wang, H. Zeng and Z. K. Xu, *Chem. Sci.*, 2022, **13**, 1698–1705.
- 34 Y. Ding, L. T. Weng, M. Yang, Z. Yang, X. Lu, N. Huang and Y. Leng, *Langmuir*, 2014, **30**, 12258–12269.
- 35 V. Ball, D. Del Frari, V. Toniazio and D. Ruch, *J. Colloid Interface Sci.*, 2012, **386**, 366–372.
- 36 V. Ball, *Biointerphases*, 2014, **9**, 030801.
- 37 C. Zhang, Y. Ou, W. X. Lei, L. S. Wan, J. Ji and Z. K. Xu, *Angew. Chem., Int. Ed.*, 2016, **55**, 3054–3057.
- 38 D. Ha and K. Kang, *ACS Omega*, 2022, **7**, 773–779.
- 39 M. L. Alfieri, L. Panzella, S. L. Oscurato, M. Salvatore, R. Avolio, M. E. Errico, P. Maddalena, A. Napolitano and M. D'Ischia, *Biomimetics*, 2018, **3**, 26.
- 40 K. B. Stark, J. M. Gallas, G. W. Zajac, M. Eisner and J. T. Golab, *J. Phys. Chem. B*, 2003, **107**, 11558–11562.
- 41 M. Gauden, A. Pezzella, L. Panzella, A. Napolitano, M. d'Ischia and V. Sundstrom, *J. Phys. Chem. B*, 2009, **113**, 12575–12580.
- 42 M. d'Ischia, O. Crescenzi, A. Pezzella, M. Arzillo, L. Panzella, A. Napolitano and V. Barone, *Photochem. Photobiol.*, 2008, **84**, 600–607.
- 43 J. B. Nofsinger, S. E. Forest, L. M. Eibest, K. A. Gold and J. D. Simon, *Pigm. Cell Res.*, 2000, **13**, 179–184.
- 44 P. Winterwerber, S. Harvey, D. Y. W. Ng and T. Weil, *Angew. Chem., Int. Ed.*, 2020, **59**, 6144–6149.
- 45 Y. Zou, X. Chen, P. Yang, G. Liang, Y. Yang, Z. Gu and Y. Li, *Sci. Adv.*, 2020, **6**, eabb4696.
- 46 T. G. Barclay, H. M. Hegab, S. R. Clarke and M. Ginic-Markovic, *Adv. Mater. Interfaces*, 2017, **4**, 1601192.
- 47 Y. Lv, H. Ma, D. Gao, Y. Zhong, H. Xu and Z. Mao, *J. Adhes. Sci. Technol.*, 2013, **27**, 81–89.
- 48 M. R. Hormozi-Nezhad, A. Moslehipour and A. Bigdeli, *Sens. Actuators, B*, 2017, **243**, 715–720.
- 49 S. K. Sharma, G. Durand and B. Pucci, *Des. Monomers Polym.*, 2012, **14**, 499–513.
- 50 A. Thompson, E. J. Land, M. R. Chedekel, K. V. Subbarao and T. G. Truscott, *Biochim. Biophys. Acta*, 1985, **843**, 49–57.
- 51 C. Nieto, M. A. Vega, J. Enrique, G. Marcelo and E. M. Martin Del Valle, *Cancers*, 2019, **11**, 1679.
- 52 M. J. Mitchell, M. M. Billingsley, R. M. Haley, M. E. Wechsler, N. A. Peppas and R. Langer, *Nat. Rev. Drug Discovery*, 2021, **20**, 101–124.
- 53 J. K. Patra, G. Das, L. F. Fraceto, E. V. R. Campos, M. D. P. Rodriguez-Torres, L. S. Acosta-Torres, L. A. Diaz-Torres, R. Grillo, M. K. Swamy, S. Sharma, S. Habtemariam and H. S. Shin, *J. Nanobiotechnol.*, 2018, **16**, 71.
- 54 S. Behzadi, V. Serpooshan, W. Tao, M. A. Hamaly, M. Y. Alkawareek, E. C. Dreaden, D. Brown, A. M. Alkilany, O. C. Farokhzad and M. Mahmoudi, *Chem. Soc. Rev.*, 2017, **46**, 4218–4244.
- 55 J. J. Rennick, A. P. R. Johnston and R. G. Parton, *Nat. Nanotechnol.*, 2021, **16**, 266–276.
- 56 J. Liebscher, *Eur. J. Org. Chem.*, 2019, 4976–4994.
- 57 J. Liu, C. Zou, C. Chen, H. Fang, Q. Wu, H. Yu, J. Zhu, L. Li, S. Yang and W. Huang, *Talanta*, 2020, **219**, 121285.
- 58 X. Wang, J. Zhang, H. Li, R. Zhang, X. Yang, W. Li, Z. Li, Z. Gu and Y. Li, *ACS Appl. Mater. Interfaces*, 2024, **16**, 22493–22503.
- 59 T. Eom, V. Barat, A. Khan and M. C. Stuparu, *Chem. Sci.*, 2021, **12**, 4949–4957.
- 60 P. Zhou, Y. Deng, B. Lyu, R. Zhang, H. Zhang, H. Ma, Y. Lyu and S. Wei, *PLoS One*, 2014, **9**, e113087.
- 61 S. Hong, Y. S. Na, S. Choi, I. T. Song, W. Y. Kim and H. Lee, *Adv. Funct. Mater.*, 2012, **22**, 4711–4717.
- 62 P. Yang, F. Zhu, Z. Zhang, Y. Cheng, Z. Wang and Y. Li, *Chem. Soc. Rev.*, 2021, **50**, 8319–8343.
- 63 Y. Xu, J. Hu, J. Hu, Y. Cheng, X. Chen, Z. Gu and Y. Li, *Prog. Polym. Sci.*, 2023, **146**, 101740.

